



**HAL**  
open science

# Fluence perturbation from fiducial markers due to edge-scattering measured with pixel sensors for $^{12}\text{C}$ ion beams

Claire-Anne Reidel, Christoph Schuy, Felix Horst, Swantje Ecker, Christian Finck, Marco Durante, Uli Weber

## ► To cite this version:

Claire-Anne Reidel, Christoph Schuy, Felix Horst, Swantje Ecker, Christian Finck, et al.. Fluence perturbation from fiducial markers due to edge-scattering measured with pixel sensors for  $^{12}\text{C}$  ion beams. *Physics in Medicine and Biology*, 2020, 10.1088/1361-6560/ab762f. hal-02493062

**HAL Id: hal-02493062**

**<https://hal.science/hal-02493062>**

Submitted on 27 Feb 2020

**HAL** is a multi-disciplinary open access archive for the deposit and dissemination of scientific research documents, whether they are published or not. The documents may come from teaching and research institutions in France or abroad, or from public or private research centers.

L'archive ouverte pluridisciplinaire **HAL**, est destinée au dépôt et à la diffusion de documents scientifiques de niveau recherche, publiés ou non, émanant des établissements d'enseignement et de recherche français ou étrangers, des laboratoires publics ou privés.

ACCEPTED MANUSCRIPT • OPEN ACCESS

## Fluence perturbation from fiducial markers due to edge-scattering measured with pixel sensors for $^{12}\text{C}$ ion beams

To cite this article before publication: Claire-Anne Reidel *et al* 2020 *Phys. Med. Biol.* in press <https://doi.org/10.1088/1361-6560/ab762f>

### Manuscript version: Accepted Manuscript

Accepted Manuscript is “the version of the article accepted for publication including all changes made as a result of the peer review process, and which may also include the addition to the article by IOP Publishing of a header, an article ID, a cover sheet and/or an ‘Accepted Manuscript’ watermark, but excluding any other editing, typesetting or other changes made by IOP Publishing and/or its licensors”

This Accepted Manuscript is © 2020 Institute of Physics and Engineering in Medicine.

As the Version of Record of this article is going to be / has been published on a gold open access basis under a CC BY 3.0 licence, this Accepted Manuscript is available for reuse under a CC BY 3.0 licence immediately.

Everyone is permitted to use all or part of the original content in this article, provided that they adhere to all the terms of the licence <https://creativecommons.org/licenses/by/3.0>

Although reasonable endeavours have been taken to obtain all necessary permissions from third parties to include their copyrighted content within this article, their full citation and copyright line may not be present in this Accepted Manuscript version. Before using any content from this article, please refer to the Version of Record on IOPscience once published for full citation and copyright details, as permissions may be required. All third party content is fully copyright protected and is not published on a gold open access basis under a CC BY licence, unless that is specifically stated in the figure caption in the Version of Record.

View the [article online](#) for updates and enhancements.

# Fluence perturbation from fiducial markers due to edge-scattering measured with pixel sensors for $^{12}\text{C}$ ion beams

Claire-Anne Reidel<sup>1,2</sup>, Christoph Schuy<sup>1</sup>, Felix Horst<sup>1,3</sup>, Swantje Ecker<sup>4</sup>, Christian Finck<sup>2</sup>, Marco Durante<sup>1</sup> and Uli Weber<sup>1</sup>

<sup>1</sup>GSI Helmholtzzentrum für Schwerionenforschung GmbH, Planckstrasse 1, 64291 Darmstadt, Germany

<sup>2</sup>Université de Strasbourg, CNRS, IPHC UMR 7871, F-67000 STRASBOURG, France

<sup>3</sup>Institute of Medical Physics and Radiation Protection (IMPS), THM University of Applied Sciences Giessen, Germany

<sup>4</sup>Heidelberger Ionenstrahl-Therapiezentrum HIT Betriebs-GmbH, Universitätsklinikum Heidelberg, Germany

E-mail: c.schuy@gsi.de

October 2019

**Abstract.** Fiducial markers are nowadays a common tool for patient positioning verification before radiotherapy treatment. These markers should be visible on X-ray projection imaging, produce low streak artifacts on CTs and induce small dose perturbations due to edge-scattering effects during the ion-beam therapy treatment. In this study, the latter effect was investigated and the perturbations created by the markers were evaluated with a new measurement method using a tracker system composed of six CMOS pixel sensors. The present method enables the determination of the particle trajectory before and after the target. The experiments have been conducted at the Marburg Ion Therapy Center with carbon ion beams and the measurement concept was validated by comparison with radiochromic films. This work shows that the new method is very efficient and precise to measure the perturbations due to fiducial markers with a tracker system. Three dimensional fluence distributions of all particle trajectories were reconstructed and the maximum cold spots due to the markers and their position along the beam axis were quantified. In this study, four small commercial markers with different geometries and materials (gold and carbon-coated  $\text{ZrO}_2$ ) were evaluated. The gold markers showed stronger perturbations than the lower density ones. However, it is important to consider that low density and low atomic number fiducial markers are not always visible on X-ray projections.

*Keywords:* Fiducial markers, MIMOSA28, CMOS pixel detector, Ion-beam therapy  
Submitted to: *Phys. Med. Biol.*

## 1. Introduction

During the past years, advanced techniques for radiotherapy treatments have been developed to give a more conformal dose to the tumor and spare the healthy tissues. One of the most important steps before starting any external radiation treatment is the precise positioning of the patient compared to the absolute coordinate system of the treatment room, especially for ion beams due to their highly conformal dose distribution (Bragg peak at the end of the range and sharp lateral fall-off) (Schardt et al. 2010). Since range uncertainties have a stronger impact for ion than photon beams, a mispositioning of the patient can lead to strong under- and overdosage in the tumor and healthy tissues respectively. This could cause an underkill of the tumor cells and/or that organs at risk (OAR) receive unwanted doses.

Between two fractions, the tumor can move due to anatomical changes. For instance, several studies showed that the prostate may move in the range 0–2 cm during the treatment (Balter et al. 1995, Crook et al. 1995, Ten Haken et al. 1991) due to the filling of the bladder and the rectum with an average displacement of around 5 mm. To verify the interfractional movement of the tumor, fiducial markers are used for image guidance and need to be visible on three dimensional (3D) imaging such as cone beam computed tomography (CBCT) and the two dimensional (2D) kilovoltage X-ray projection imaging. The markers are surgically implanted inside or at the border of the tumor before the treatment and are used to compare the tumor position determined on the treatment planning CT and its position during the daily treatment determined most of the time by X-ray projections. The spatial stability of the fiducial markers was investigated by Kupelian et al. (2005) with two or three implanted markers. In 99% of all cases the movement of the markers was smaller than 4 mm.

Fiducial markers are generally composed of materials with density and atomic number high enough to be visible on different imaging methods such as CBCT or X-ray projections (Habermehl et al. 2013). However, as shown in previous studies (Cheung et al. 2010, Habermehl et al. 2013), fiducial markers can cause image artifacts on the treatment planning CT. Therefore it is important that the markers are small enough or with low densities to avoid significant streak artifacts on the CT recorded before the patient treatment.

The dose perturbation induced by fiducial markers is due to inhomogeneous scattering when a particle beam passes a strong density gradient perpendicularly to the beam. The angular distribution  $\sigma_\alpha$  from the multiple Coulomb scattering can be estimated by the Highland approximation (Highland 1975, 1979) and depends on the projectile type and energy as well as on the atomic number and the density of the material. It is important to note that protons scatter 3.5 times more than carbon ions for the same range.

During the last years, mainly high density (e.g. gold) and relatively large diameter ( $> 1$  mm) markers were used for position verification since they can easily be seen on the X-ray projection. However, these types of markers induce significant artifacts on CT (Habermehl et al. 2013) and also cause cold/hot spots (dose perturbations) during

the treatment due to inhomogeneous scattering of the ion beam. Other markers with lower density and atomic number (e.g. carbon-coated  $\text{ZrO}_2$  marker) would reduce these inhomogeneities created by the markers. However, they are not always visible on the X-ray projections performed during the daily treatment.

Several studies investigated the severeness of the dose perturbations induced by fiducial markers with Monte Carlo (MC) simulations (Newhauser et al. 2007, Giebeler et al. 2009, Herrmann et al. 2010) and/or measurements with radiochromic films (Cheung et al. 2010, Huang et al. 2011). These studies have shown that the dose perturbations depend on the marker material, thickness, position inside the phantom and orientation. The bigger and heavier the material is, the stronger is the scattering effect which creates larger and stronger cold and hot spots. Another MC simulation study showed that the dose perturbation due to the markers could be partly reduced using several fields (Matsuura et al. 2012). The measurements performed with radiochromic films were mainly done for protons and with several films placed along the beam axis. However, it is difficult to predict where to place them exactly along the longitudinal axis to precisely measure the maximum dose perturbation induced by the markers.

In this work, a new concept for measuring these dose perturbations was proposed and validated. The experimental setup consists of a silicon tracking system with six MIMOSA28 pixel detectors of high spatial resolution (Valin et al. 2012). With this method, the fluence is measured and each particle trajectory is reconstructed with high spatial resolution. After reconstruction of all tracks, a 3D fluence distribution is computed. The maximum perturbation induced by the markers can then be determined as well as its position along the beam axis. This method has therefore the advantage to seamlessly compute these perturbations along the beam axis from a reconstructed 3D fluence distribution which is not possible with radiochromic films. Another advantage of the present method is that the maximum perturbations can be measured without knowing their position along the beam axis in advance. As investigated in the previous studies, the perturbations induced by the fiducial markers depend on many different parameters. The gold markers investigated in this work have a diameter  $\leq 0.5$  mm since it was shown by Habermehl et al. (2013) that bigger gold markers are not recommended to be used in ion-beam therapy. The spatial resolution of the tracks is smaller than  $10 \mu\text{m}$ , which provides good information about the fluence perturbations not only at a certain  $z$  position but also along the beam axis by extrapolation. The presented measurement campaign was conducted at the Marburg Ion Therapy Center (MIT) in Germany with carbon ion beam at three different energies and with four different fiducial markers. Even though protons show stronger scattering effects,  $^{12}\text{C}$  ions were chosen in this work since fewer studies have been performed for these ions. Moreover, the challenge of quantifying the perturbation is higher since the effect is smaller. To benchmark the results obtained from the tracker, the dose perturbations were additionally measured using radiochromic films.

**Table 1.** Properties of the different fiducial markers used for the beam experiments.

Name	Manufacturer	Material	Shape	Length (mm)	Diameter (mm)	Mass (mg)
Visicoil	IBA	Gold	coil-shaped	20	0.5	24
Gold Anchor #1	Naslund Medical AB	Gold	straight	11 <sup>a</sup>	0.28	9 <sup>b</sup>
Gold Anchor #2	Naslund Medical AB	Gold	folded	2.5 <sup>c</sup>	0.28	14 <sup>d</sup>
Acculoc Carbon marker	Carbon Medical Technologies	ZrO <sub>2</sub> (carbon-coated)	bone-shaped	3	1	5.5

<sup>a</sup>nominal length: 10 mm

<sup>b</sup>nominal mass: 8 mg

<sup>c</sup>unfolded: 17.5 mm, nominal length: 20 mm

<sup>d</sup>nominal mass: 17 mg

## 2. Material & Methods

### 2.1. Fiducial markers

In this work, four common fiducial markers were selected to evaluate the induced fluence perturbation inside the target volume. They are listed in Table 1.

### 2.2. MIMOSA28 pixel sensor & Software analysis

The MIMOSA28 (Minimum Ionizing MOS Active pixel sensor) detector based on CMOS technology is a high spatial resolution pixel sensor (Valin et al. 2012). This detector has an area of  $\sim 2 \times 2 \text{ cm}^2$  and is composed of 928 rows  $\times$  960 columns with squared pixels of  $20.7 \mu\text{m}$  length. The total thickness of the sensor is  $50 \mu\text{m}$  with an epitaxial layer of  $14 \mu\text{m}$ . Each pixel delivers a binary output after discrimination of the signal and the whole sensor has a readout time of  $186.5 \mu\text{s}$  ( $\sim 5 \text{ kHz}$  frame rate).

When the particle passes through the sensors, charges produced by ionization are collected by a certain number of pixels in the sensor. The analysis software QAPIVI (Finck et al. 2017), based on the ROOT (Brun & Rademakers 1996) and GEANT4 (Agostinelli et al. 2003) libraries, reconstructs the groups of fired pixels (clusters). By calculating the cluster position defined as the center of mass of the fired pixels, a straight line matching the clusters in the different sensors (also referred to as *plane*) is reconstructed (tracking). The latter was performed with the original algorithm from QAPIVI with improvements based on multiple Coulomb scattering. Finally, the vertices of the tracks when a target is placed in front or in-between the tracker are computed. In this work, the vertexing was not performed since the needed information for the analysis was provided by the tracks from the last 3 sensors (see Section 2.6). The resolution of a single track is better than  $10 \mu\text{m}$  and the performance of these algorithms are described in the study from Rescigno et al. (2014). In order to attain this track resolution, it

is necessary to align the sensors. The mechanical mispositioning of the sensors can be precisely corrected by software with an alignment procedure (Reidel et al. 2019). For the alignment of the sensors, a specific run without target is needed.

### 2.3. Radiochromic films

The validation of the experiment was performed with radiochromic films (GAFCHROMIC EBT3, Lot#: 06141702). These films have a total thickness of  $278 \mu\text{m}$  and an active layer of  $28 \mu\text{m}$  and are resistant to water for short time immersion (León-Marroquín et al. 2018). The films were cut in pieces of  $6.4 \times 6.8 \text{ cm}^2$  and were protected with tape around the borders to prevent damage due to the water. During the irradiation, the films were all placed in portrait orientation to avoid any changes in the film response due to its orientation (Schoenfeld et al. 2016). The EBT3 films were then scanned after several hours using a VIDAR scanner (Dosimetry Pro Advantage) with a spatial resolution of 300 dpi ( $\sim 85 \mu\text{m}$ ) and 16 bits resolution in portrait orientation (Borca et al. 2013). Before the film analysis, a calibration curve needed to be measured. Therefore, a film from the same batch was irradiated with 8 different scanned squares receiving a given fluence within a range of  $5 \times 10^6 - 3 \times 10^9 \text{ ions/cm}^2$ , corresponding to a dose range of around  $0 - 70 \text{ Gy}$  considering also the film background. The gray values of the film were then calibrated to the given fluence and each irradiated film could be analyzed by using the established calibration curve. The images from the films were processed by using the software ImageJ (Schneider et al. 2012).

### 2.4. Experimental setup

The measurements were conducted at MIT where the two different methods were applied to determine the inhomogeneous scattering induced by fiducial markers: on the one hand with the MIMOSA28 pixel sensors and on the other hand with EBT3 radiochromic films. The latter were used to validate the new concept of measuring the fluence perturbations with a tracker system. The two experiments were conducted with few months in-between. In order to perform clinically relevant measurements, each fiducial marker was placed inside a small water aquarium of 4 cm length and positioned at the isocenter. To improve their handling, the markers were glued to a thin polyethylene (referred to as *PE*) plate of 1 mm thickness. The markers were positioned along the vertical axis perpendicular to the beam. In addition, a PE block of 9 cm length was placed in front of the water aquarium to simulate the healthy tissues of a patient. The beam energies were chosen in order to cover a range of 3 cm (slightly smaller than the length of the water aquarium). The energies, Full Width Half Maximum (FWHM) and the range in water of the carbon ion beams used during the experiments at MIT are listed in Table 2. The energies and FWHM at isocenter position were assumed as the nominal values from MIT (ensured by the regular QA) while the ranges were calculated with LISE++ (Tarasov & Bazin 2008). The Water Equivalent Path Length (WEPL) of the experimental setup (computed with LISE++) was about 140 mm. The total range of

**Table 2.** Beam energy, FWHM at the isocenter and range in water (calculated with LISE++) of the carbon ion beams used for the experimental measurements.

Energy (MeV/u)	FWHM (mm)	Range in water (mm)
278.84	5.6	150.4
294.97	5.5	165.1
310.61	5.4	179.9

the different ion beams used in the experiment was chosen to have enough energy to pass through the PE block, the water aquarium and the sensors placed after the water aquarium (see Figure 1(b) in Section 2.4.1).

*2.4.1. CMOS measurements* To measure the fluence perturbation due to the fiducial markers, a tracker system of six MIMOSA28 pixel sensors was placed at  $0^\circ$  with respect to the beam axis. A 5 mm plastic scintillator (BC-400) was placed in front of the sensors to monitor the beam intensity by counting the incoming particles. Several beam profile measurements along the beam axis were performed to be able to properly align the sensors (as mentioned in Section 2.2) and to verify the measurements with other techniques (e.g. radiochromic films). Two sets of three sensors were placed on each side of the PE block (see Figure 1(a)). The beam profiles were measured with and without the PE block. The two sets of sensors were then moved to each side of the water aquarium (see Figure 1(b)). As before, a measurement with and without the PE block and the water aquarium was performed. In the second part of the experiment, the fiducial markers were inserted in the water aquarium as explained above. The first 3 sensors were used for monitoring the constancy of the beam profile while the 3 last sensors were used to measure the fluence perturbation due to the marker.

*2.4.2. Radiochromic film measurements* The dose perturbations due to the fiducial markers were also measured with EBT3 radiochromic films (described in Section 2.3). They were positioned in a similar configuration as the experiment described in Section 2.4.1 in order to validate the measurement concept with a tracker system. As for the CMOS experiment, the films were placed along the beam axis as shown in Figure 2. The films at position  $i$  are later referred to as  $Fi$ . A 5 mm plastic plate was placed in front of the first film to simulate the 5 mm plastic scintillator used during the CMOS experiment. The same set of measurements was conducted: the beam profiles without any perturbations were measured without the 5 mm plastic, the PE block and the water aquarium. They were then measured with the 5 mm plastic, the PE block and the water aquarium. The perturbation from the fiducial markers were then measured after placing the marker inside the water aquarium at the isocenter position (Figure 2) by using the same method as described in Section 2.4.1. For the latter measurement, an additional film was placed inside the aquarium at 5 mm before the marker. This film

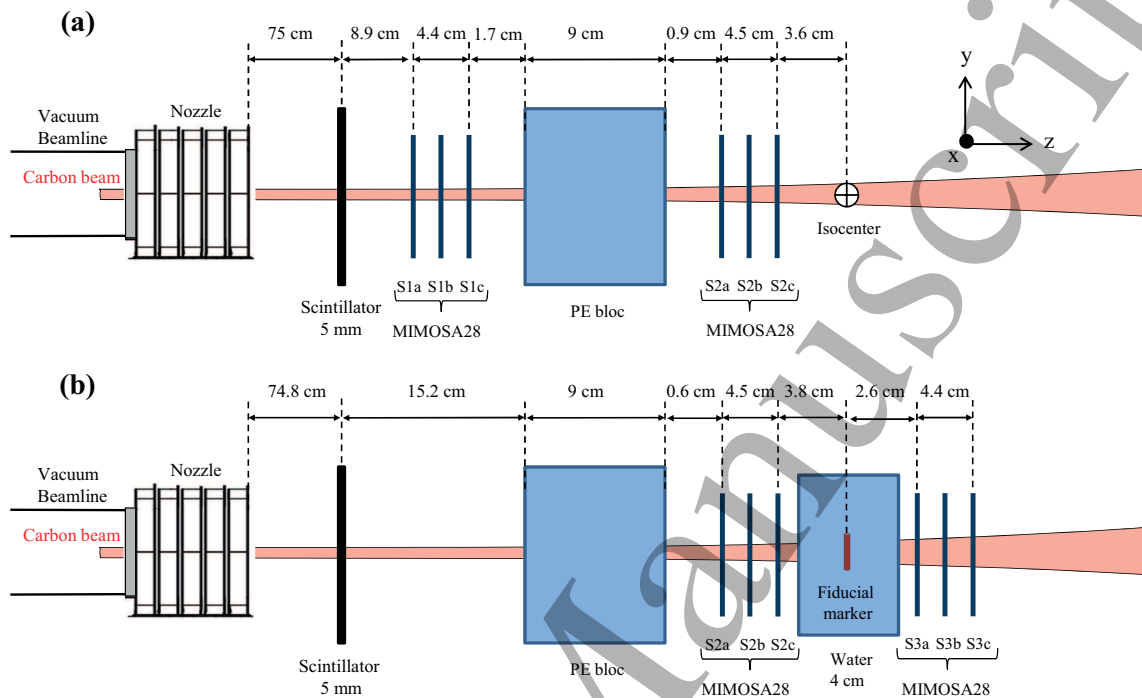


**Figure 1.** Both configurations (panels (a) and (b)) used during the experiment to measure the fluence perturbation due to fiducial markers with the MIMOSA28 pixel sensors.

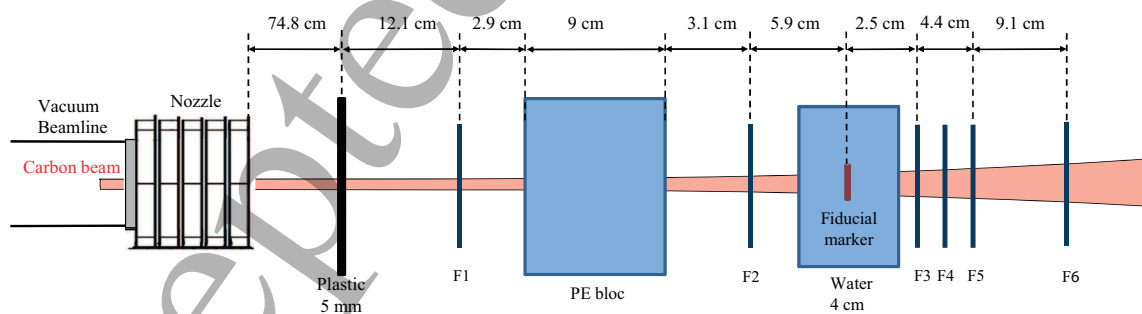


**Figure 2.** Experimental setup dedicated to the dose perturbation measurements due to fiducial markers with radiochromic films.

is not represented in Figure 2 but was used to verify the stability of the beam profile during the measurements.

### 2.5. Beam profile analysis

This analysis part aimed to benchmark the new measurement concept with a tracker system against a standard measurement method with radiochromic films. In a first step, beam profile measurements were performed without perturbation and in a second step with the fiducial markers for the CMOS and film experiments (see Figures 1 and 2). The MIMOSA28 sensors and radiochromic film data were processed as explained in Section 2.2 and Section 2.3 respectively. From the reconstructed tracks, a 2D beam profile  $(x, y)$  can be extracted at any position along the  $z$ -axis. For both experiments, the beam profiles in  $x$  and  $y$  are obtained by integrating the distribution over the perpendicular directions  $y$  and  $x$  respectively. Without perturbation due to the markers, the profiles were integrated over the full distribution. However, in the case that a fiducial marker was placed inside the aquarium, the profiles in  $x$  were integrated over a smaller area in  $y$  that correlates to the length of the marker in order to evaluate its perturbation. The data sets from the tracker and the films were analyzed independently and normalized as a function of the profiles integral in order to compare the measurements. The normalization and shift of each  $x$  and  $y$  beam profile was performed by means of a cumulative distribution function (also referred to as *Gaussian integral function*  $\Phi$ ). In the case of the MIMOSA28 beam profile analysis, each entry of the histogram has been weighted as a function of the cluster size (see Section 2.2). The response of the detector (number of pixels per cluster) is related to the deposited energy (Spiriti et al. 2017) from the particle passing through the detector which means also dependent on the charge of the particle. In this work, the applied weight was calculated following equation 3 of Spiriti et al. (2017). Since the absorbed dose is proportional to the deposited energy, it is possible to establish a correlation between the absorbed dose and the cluster size. However, the energy resolution of the CMOS sensor is low and the applied weight is only a rough correction to the fluence profiles obtained with the CMOS sensors in order to get a more realistic comparison with the radiochromic films.

### 2.6. Fluence distribution analysis

The goal of this analysis part is to determine the maximum cold spot and its position along the beam axis with a precise and efficient method. A 3D fluence distribution is reconstructed after performing the tracking which determines the trajectory of each single particle crossing the sensors. This distribution is computed from all tracks, which are defined by 3D vectors, reconstructed with the tracker placed after the aquarium. For this,  $10 \times 10 \times 100 \mu\text{m}^3$  voxels are computed and the fluence in each voxel is determined by the sum of all the tracks passing through this voxel. The 3D fluence distributions are therefore the scoring of the total number of intersections from the reconstructed tracks with the voxels. The 2D fluence distribution (referred to as *fluence map*) presented in this study show the propagation of the perturbation in the  $(x, z)$  planes integrated over a small area along the  $y$ -axis as it was done in Section 2.5 for the beam profiles. The integration range in  $y$ -direction was varied to test the robustness of the chosen window.

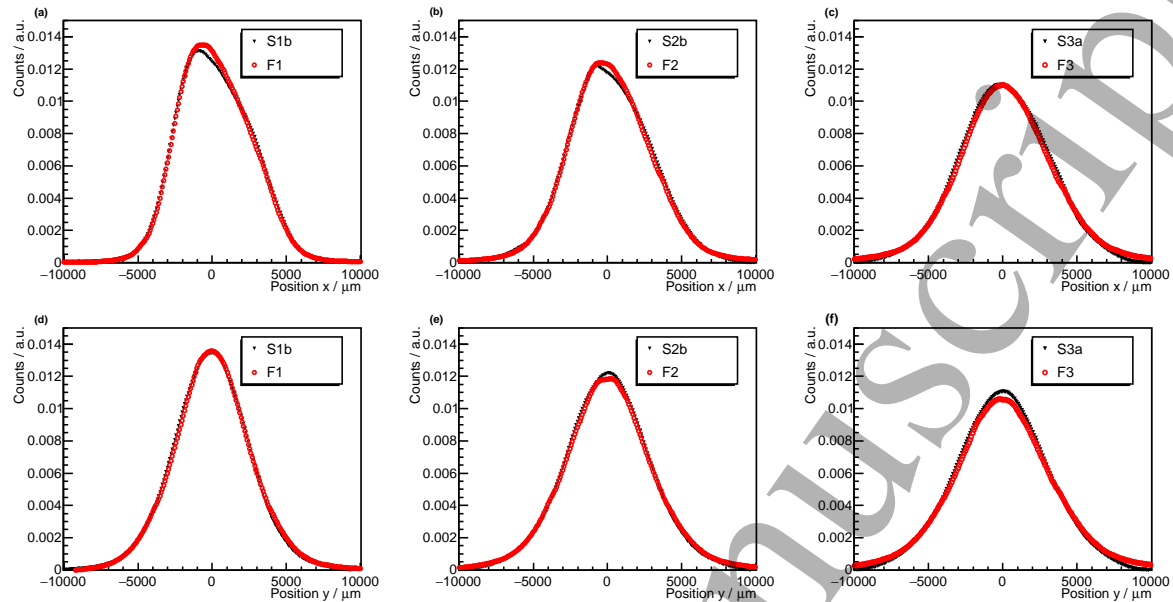


**Figure 3.** Beam profiles from the MIMOSA28 sensors and the EBT3 radiochromic films for 294.97 MeV/u carbon ion beam from the experimental measurements. Panels (a) to (c) show the profiles in  $x$  while panels (d) to (f) show the profiles in  $y$  for the MIMOSA28 sensors (inverted black triangle) and EBT3 radiochromic films (red circle) before the PE block with sensor S1b and film F1 (panels (a) and (d)), after the PE block with sensor S2b and film F2 (panels (b) and (e)) and after the water aquarium with sensor S3a and film F3 (panels (c) and (f)).

From the integrated 2D fluence map, the cold spots at any position along the beam axis can be extracted. To determine the maximum cold spot, the beam profiles with and without marker were compared.

### 3. Results

#### 3.1. Beam profiles

In this section, the beam profiles from the MIMOSA28 sensors and the film experiments were first compared without any perturbation. In order to do this, the analysis method explained in Section 2.5 was followed and the beam profiles in  $x$  and  $y$  at different positions along the beam axis were computed. Figure 3 shows the beam profiles before the PE block, after the PE block and after the water aquarium from the CMOS sensor measurements S1b, S2b and S3a superimposed with the film measurements F1, F2 and F3 respectively (see experimental setups in Figures 1 and 2). The mean value and Root Mean Square (RMS) of each profile were computed after integration over a range of  $-8000$  to  $+8000$   $\mu\text{m}$  and are listed in Table 3. The obtained results from the MIMOSA28 sensors and the films are in good agreement. Moreover, the mean value and RMS differences from the two experiments in  $x$  and  $y$  are smaller than  $50$   $\mu\text{m}$  and  $150$   $\mu\text{m}$ .

**Table 3.** Mean and RMS values of the beam profiles in  $x$  and  $y$  from the MIMOSA28 sensors and the radiochromic films at equal positions along the beam axis for 294.97 MeV/u carbon ion beam.

	Before PE		After PE		After aquarium	
	S1b	F1	S2b	F2	S3a	F3
Mean in $x$ ( $\mu\text{m}$ )	181.3	188.8	172.3	156.7	104.4	157.2
RMS in $x$ ( $\mu\text{m}$ )	2409	2372	2706	2674	2903	2973
Mean in $y$ ( $\mu\text{m}$ )	-61.8	28.0	1.8	39.4	-41.3	1.0
RMS in $y$ ( $\mu\text{m}$ )	2509	2551	2753	2837	2968	3090

### 3.2. Fiducial marker perturbations

In the following section, the fluence and dose perturbations from the MIMOSA28 sensors and radiochromic films are quantified. The EBT3 films deliver a gray level related to the absorbed dose at the measurement position whereas the CMOS pixel sensors measure the trajectory of each single particle.

*3.2.1. Perturbation comparison: CMOS sensors versus radiochromic films* Since the beam profiles without any perturbation measured with the MIMOSA28 sensors and the radiochromic films showed similar results, it is possible to compare the effect of the fiducial markers from both experiments. As previously, the analysis method described in Section 2.5 was followed. However, the length of the integrated area along the  $y$ -axis was 8 mm for the Gold Anchor #1 and the Visicoil markers and was 2.5 mm for the Gold Anchor #2 and the carbon-coated  $\text{ZrO}_2$  markers. It is important to note that the same area was used for the MIMOSA28 sensors and the radiochromic films. Since the perturbation is determined compared to the beam profiles without any perturbation, it is also necessary to integrate them over the same range. In Figure 4, the beam profiles from the sensor S3a and the film F3 with the Gold Anchor #1 are presented. The CMOS measurement shows a cold spot of 2.4% and the radiochromic film a cold spot of 2.5% for 294.97 MeV/u  $^{12}\text{C}$  ion beam.

*3.2.2. Fluence perturbation measured with CMOS sensors* Since the fluence perturbation from the fiducial markers is induced by multiple Coulomb scattering, the perturbation varies along the beam axis. A maximum cold spot is present at a certain  $z$  position which is difficult to precisely predict before the analysis of the experimental data. In this section, the results of the maximum perturbation due to the fiducial markers are computed from the fluence map of all reconstructed tracks as explained in Section 2.6. The fluence maps were integrated over a determined area as for the analysis in Section 3.2.1. To determine the maximum cold spot, the beam

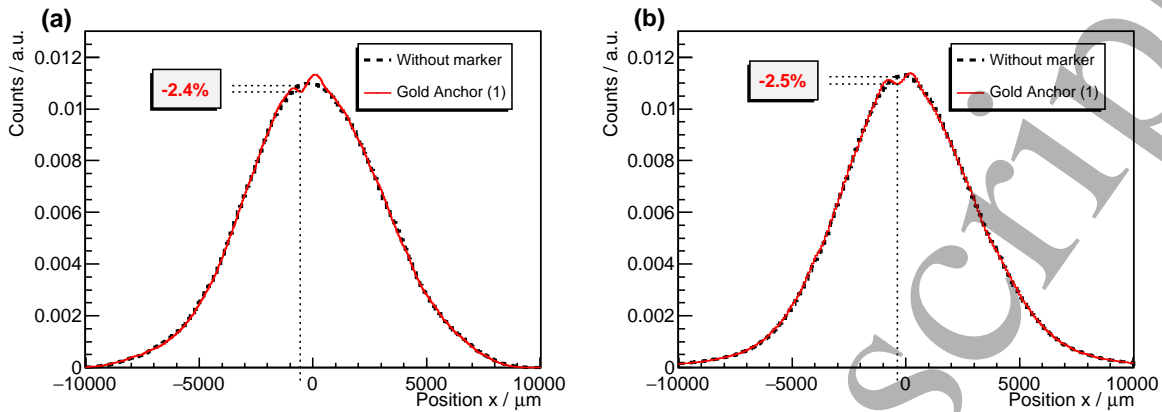


**Figure 4.** Beam profiles in  $x$  from the MIMOSA28 sensor S3a (panel (a)) and the EBT3 radiochromic film F3 (panel (b)) without any perturbation (black dashed line) and when the Gold Anchor #1 is placed inside the water aquarium (red line) for 294.97 MeV/u carbon ion beam from experimental measurements. The vertical dotted line indicates the position in  $x$  of the maximum perturbation while the dotted horizontal lines quantify the cold spot from the profiles with and without perturbation at this position.

profile when the marker is introduced inside the water aquarium was compared to the beam profile without marker for the same integrated area at the same position along the beam axis. In Figures 5, 6 and 7, the fluence maps and the corresponding profiles from the maximum cold spots are shown for the Gold Anchor #1, the Visicoil and the carbon-coated  $\text{ZrO}_2$  fiducial markers for each of the three energies for carbon ion beam. It is important to note that the zero positions in  $x$  and in  $z$  are the coordinates of the fiducial marker position. A summary of the maximum cold spot values from the fiducial markers and their corresponding position along the beam axis are listed in Table 4. The uncertainties on the maximum cold spot values were calculated as the quadratic sum from the uncertainty on the beam profiles with and without marker. The relative uncertainty on a single beam profile was calculated as  $1/\sqrt{N}$ , with  $N$  the total number of entries at the  $x$  position where the maximum cold spot was determined. The uncertainty on the  $z$  position where the maximum cold spot is present was determined as 3 mm comprising the uncertainty from the sensor positioning and the uncertainty on the reconstructed track. The integration range in  $y$ -direction was varied to benchmark the robustness of the chosen window. The results obtained with the different windows were in good agreement. The values from Table 4 show that the maximum cold spots and their position vary as a function of the markers and the primary beam energy. Smaller the energy is, stronger is the effect from marker. Moreover, markers with high density and high atomic number create stronger and larger cold spots.

In this work, the Gold Anchor #2 (see Table 1) was also analyzed. This fiducial marker is more complex since it is folded in a random shape. Moreover, the area in which the tracks were integrated is small compared to the Gold Anchor #1. In Figure 8, the fluence map and the beam profile at the maximum cold spot position is shown for

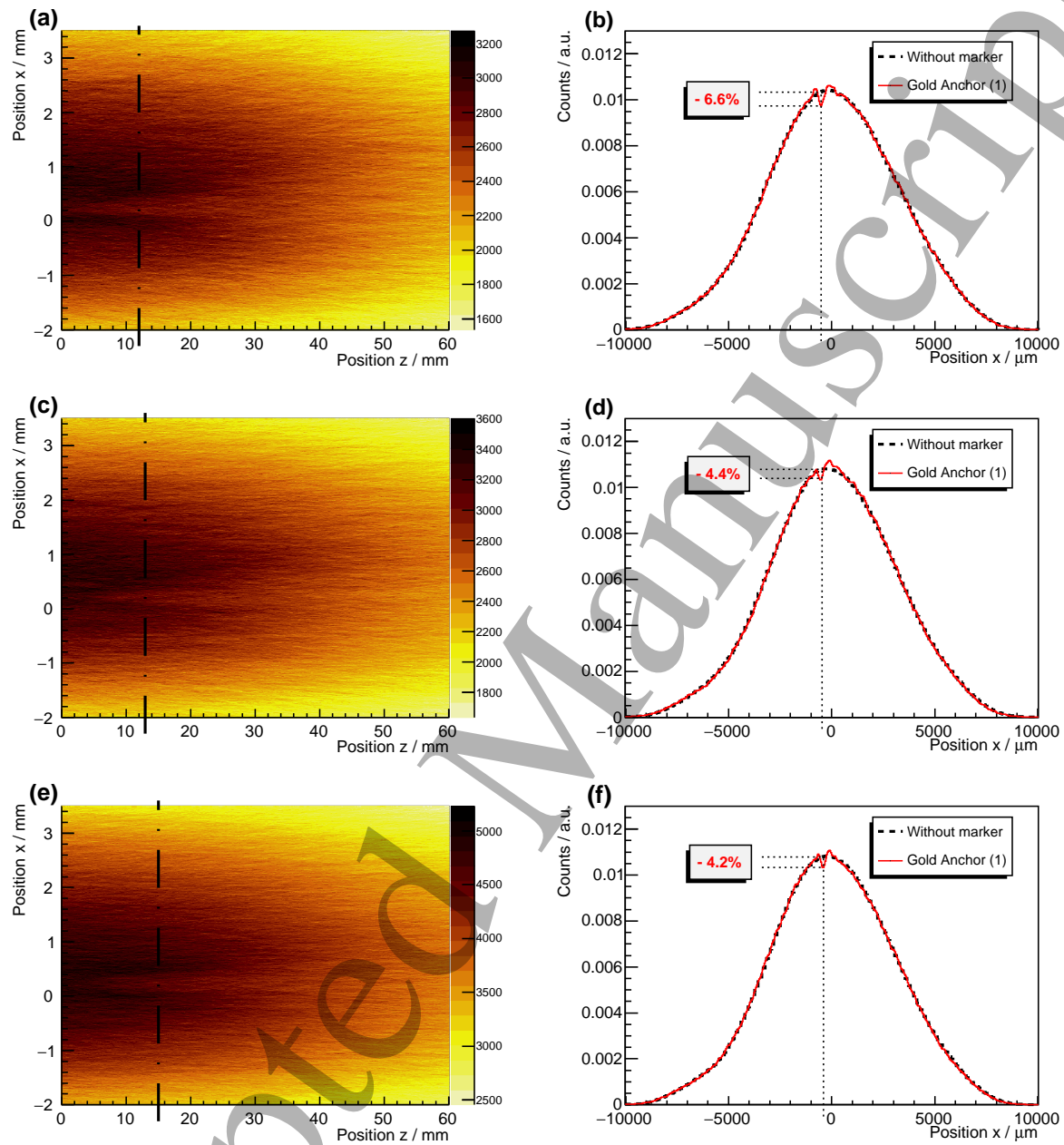


**Figure 5.** Reconstructed fluence maps and beam profiles of carbon ions at three different energies through the Gold Anchor #1 marker placed at position zero along the  $z$ -axis and the  $x$ -axis. Panels (a), (c) and (e) show the fluence maps reconstructed from all tracks and panels (b), (d) and (f) show their corresponding profile at the  $z$  position where the perturbation is maximum for 278.84 (panels (a) and (b)), 294.97 (panels (c) and (d)) and 310.61 MeV/u (panels (e) and (f)) carbon ion beams from the experimental measurements. The black vertical dash-dotted line on the fluence map represents the corresponding position along the beam axis where the cold spot is maximum. In panels (b), (d) and (f), the red line shows the profile at this position when the marker is placed inside the water aquarium while the black dashed line shows the profile when there is no perturbation for the same  $z$  position. In the same panels, the vertical dotted line indicates the position in  $x$  of the maximum perturbation while the dotted horizontal lines quantify the cold spot from the profiles with and without perturbation at this position.

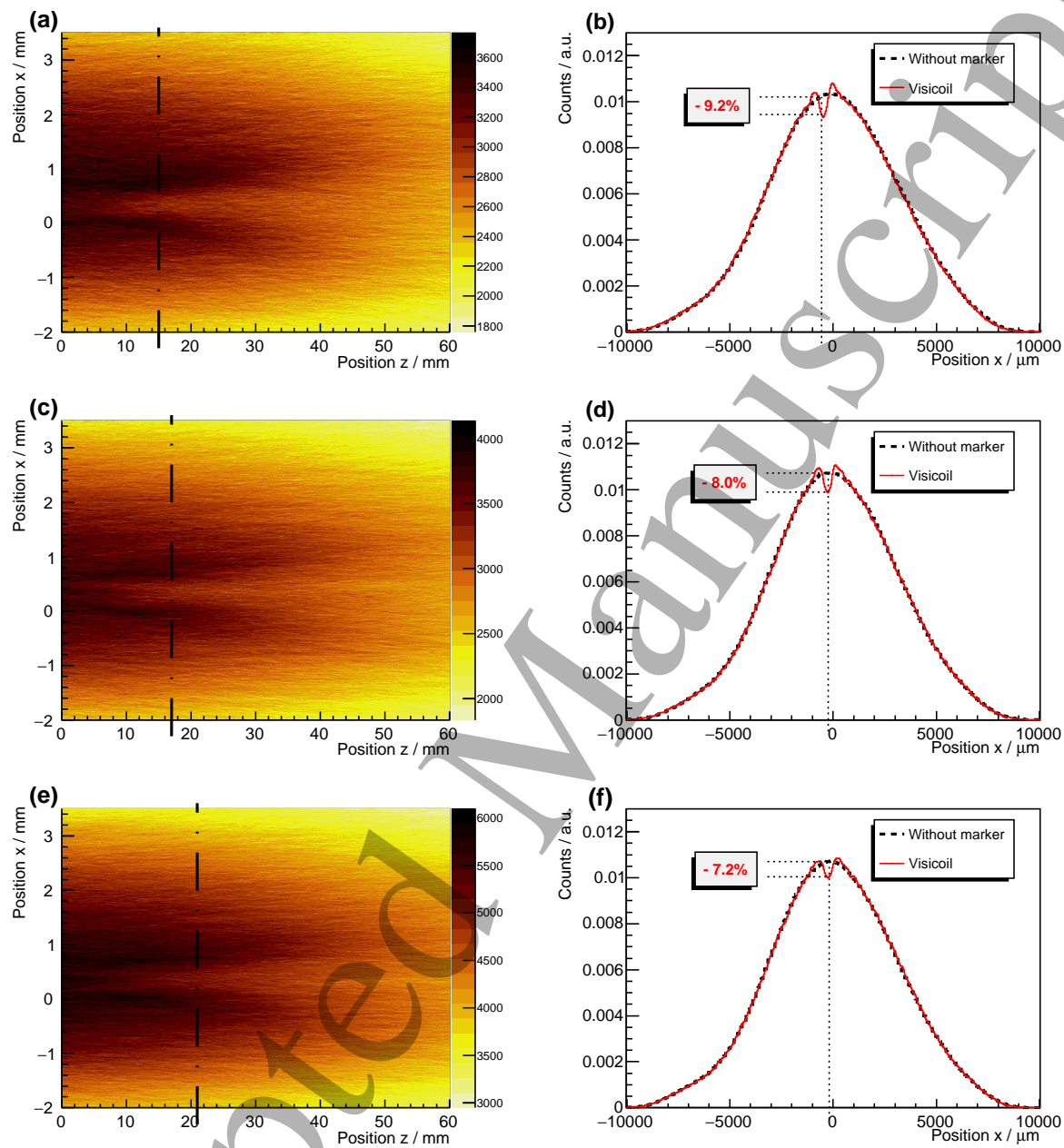


**Figure 6.** Reconstructed fluence maps and beam profiles of carbon ions at three different energies through the Visicoil marker placed at position zero along the  $z$ -axis and the  $x$ -axis. The panels description is the same as Figure 5.

310.61 MeV/u carbon ions. The cold spot created by the Gold Anchor #2 is about 4.4%.

#### 4. Discussion

The fiducial markers studied in this work are in use for image guidance during ion-beam therapy cancer treatment. Different criteria need to be taken into account for

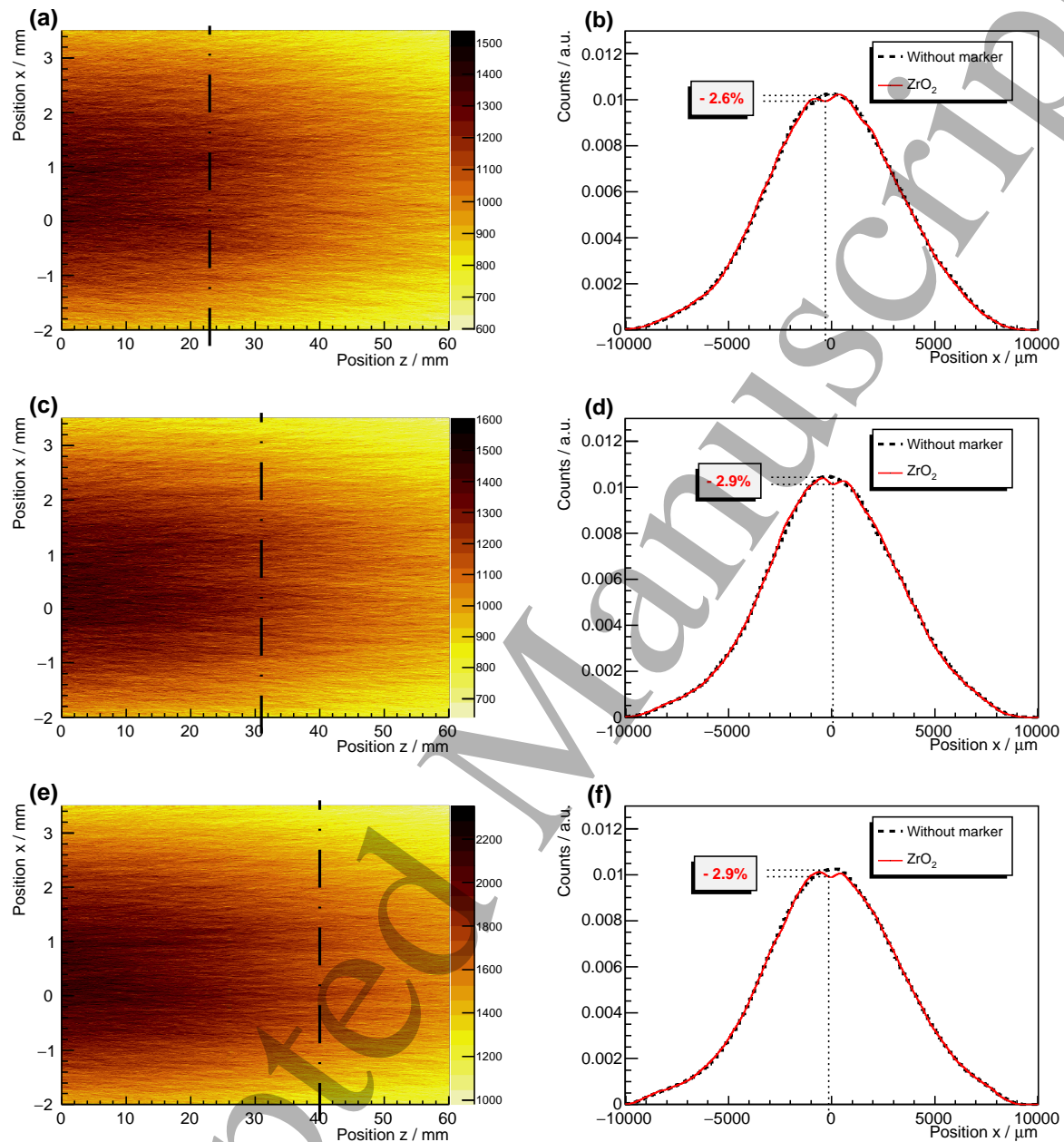


**Figure 7.** Reconstructed fluence maps and beam profiles of carbon ions at three different energies through the carbon-coated  $\text{ZrO}_2$  marker placed at position zero along the  $z$ -axis and the  $x$ -axis. The panels description is the same as Figure 5.

the markers such as their visibility on X-ray projections or on CBCT images, their artifacts on the treatment planning CT and their dose perturbations. In this work, the latter was evaluated with carbon ions for different small fiducial markers ( $\leq 0.5$  mm diameter for gold markers) that were designed for low dose perturbations. In order to detect these perturbations, a new measurement concept was applied. A tracker system composed of six high resolution pixel sensors was used to measure a 3D image of the fluence reconstructed from all single tracks. And the maximum perturbation from a

**Table 4.** Summary of the cold spot values where the perturbation is maximum and its position along the  $z$ -axis for the different fiducial markers for carbon ion beam at three different energies.

Energy (MeV/u)	maximum cold spot (%)			$z$ position (mm)		
	ZrO <sub>2</sub>	Gold Anchor #1	Visicoil	ZrO <sub>2</sub>	Gold Anchor #1	Visicoil
278.84	$2.8 \pm 0.7$	$6.6 \pm 0.4$	$9.2 \pm 0.4$	$23 \pm 3$	$12 \pm 3$	$15 \pm 3$
294.97	$2.9 \pm 0.7$	$4.4 \pm 0.4$	$8.0 \pm 0.4$	$31 \pm 3$	$13 \pm 3$	$17 \pm 3$
310.61	$2.9 \pm 0.6$	$4.2 \pm 0.4$	$7.2 \pm 0.4$	$40 \pm 3$	$15 \pm 3$	$21 \pm 3$

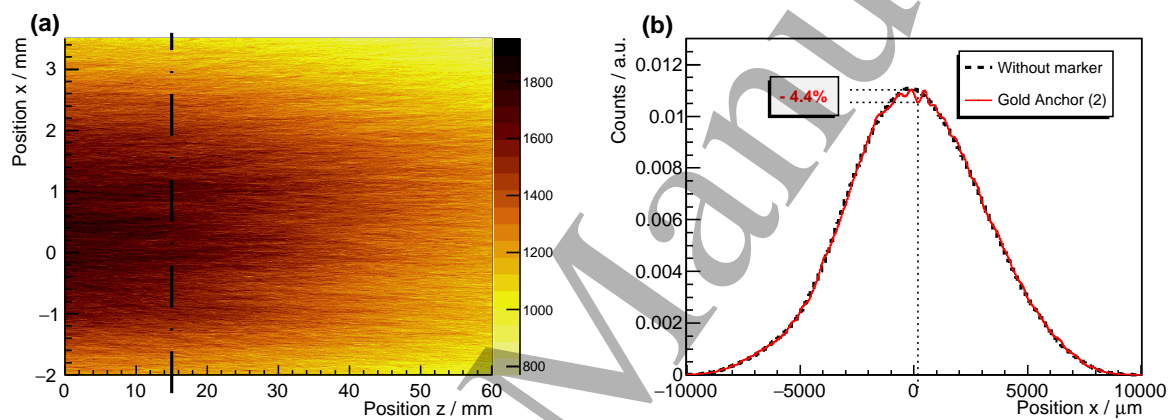


**Figure 8.** Reconstructed fluence map and beam profile for 310.61 MeV/u carbon ion beam through the the Gold Anchor #2 marker placed at position zero along the  $z$ -axis and the  $x$ -axis. Panel (a) shows the fluence map reconstructed from all tracks panel (b) shows its corresponding profile at the  $z$  position where the perturbation is maximum from the experimental measurements. The black vertical dash-dotted line on the fluence map represent the corresponding position along the beam axis where the cold spot is maximum. In panel (b), the red line shows the profile at this position when the marker is placed inside the water aquarium while the black dashed line shows the profile when there is no perturbation for the same  $z$  position. In the same panel, the vertical dotted line indicates the position in  $x$  of the maximum perturbation while the dotted horizontal lines quantify the cold spot from the profiles with and without perturbation at this position.

fiducial marker along the beam axis was evaluated for three energies of  $^{12}\text{C}$  ion beams and for four fiducial markers.

To validate this new measurement method, the experiment was repeated with radiochromic films. The latter were placed at the same positions as the MIMOSA28 sensors from the previous experiment. As shown in Figure 3, the beam profiles without any perturbation measured with the films and the CMOS sensors are in agreement. Indeed, the mean value and RMS differences from the two experiments in  $x$  and  $y$  are smaller than  $50 \mu\text{m}$  and  $150 \mu\text{m}$ . They can come from several points such as the resolution of the detectors and that the two experiments were performed with

few months in-between. Another reason for these deviations is that the radiochromic films are used to measure the deposited energy and the MIMOSA28 sensors deliver a fluence output. Even though the latter were corrected by applying a weighting factor (as explained in Section 2.5), the correction is not perfect. As it can be seen in Figure 3, the difference increases after the PE block and the water aquarium. Since the production of lighter fragments increases, the field becomes more complex and the deviation between the two measurement methods increases. In addition, light fragments (e.g. protons) are emitted at larger angles than the heavier ones. Light fragments deposit less energy and therefore the tail of the film profiles is smaller than for the CMOS sensors before applying a correction factor. With the latter measurement concept, the deposited energy from the particles passing through the detectors and their charge can be correlated to the cluster size. Due to the digital output of the MIMOSA28 sensor (Spiriti et al. 2017), it is not possible to separate clearly the different produced fragments. However, the primary  $^{12}\text{C}$  ions could be distinguished from the lighter fragments due to its well defined cluster size.

It is also important to benchmark the profiles from the CMOS sensors with the radiochromic films when a perturbation due to the fiducial marker is present. As it can be seen in Figure 4, the Gold Anchor #1 marker at the position of sensor S3a induces a cold spot of 2.4% for the MIMOSA28 sensors and a cold spot of 2.5% on the film F3 for 294.97 MeV/u  $^{12}\text{C}$  ions. The results from the CMOS sensors and the radiochromic films are in good agreement with and without perturbation. This shows that the new concept with CMOS sensors for the fluence perturbation measurements due to fiducial markers is valid.

The different markers listed in Table 1 were measured with the tracker system and analyzed with the method described in Section 2.6 for  $^{12}\text{C}$  ions at three different energies (Table 2). After reconstructing the 2D fluence map, it was possible to evaluate the cold spot created after the marker along the beam axis and to quantify the maximum cold spot and its distance downstream of the fiducial marker. The hot spots were not reported in this work even though they can also be identified. In general, a small overdosage in a small part of the target volume is considered much less critical than a local underdosage that can potentially cause a recurrence of the tumor. A good rule of thumb is that the magnitude of the two hotspots is roughly 50% of the enclosed cold spot, as can be seen in Figures 5–7. However, this also depends on the orientation of the marker to the primary beam. It is important to note that, for all measurements, the beam profile was integrated and the total area of the profiles with and without markers was found to be the same. The cold spot increases with the density and the atomic number of the marker material. The maximum cold spot created along the beam axis and its position differ for all markers since it depends on several factors such as the density, the orientation and the thickness. The beam energy also influences the perturbation since multiple Coulomb scattering depends on the projectile energy. All markers were measured in vertical position and the Gold Anchor was also measured when folded. This study shows that the Viscoil marker, which has a diameter of 0.5 mm,

induces a stronger fluence perturbation than the Gold Anchor #1 of 0.28 mm diameter. The carbon-coated  $\text{ZrO}_2$  is thicker but induces less perturbation since it is less dense. The maximum cold spots measured in this work for a 278.84 MeV/u carbon ion beam were about 6.6 and 9.2% for the Gold Anchor #1 and the Viscoil and their position downstream the fiducial marker were 13 and 15 mm respectively. For the carbon-coated  $\text{ZrO}_2$  marker, the perturbation was found to be  $< 3\%$  for all energies. Therefore it could be a good candidate for image guidance during carbon ion therapy treatments. However, since it has a lower density than gold markers, it can be difficult to see it on X-ray projections. For instance, at the Heidelberg Ion Therapy Center (HIT) in Germany, the Gold Anchor is used for proton therapy treatments of prostate cancer. In contrast to the gold markers, the carbon-coated  $\text{ZrO}_2$  marker is not visible on the daily X-ray imaging at HIT.

The measurements presented in this work were performed with a setup where the pixel sensors were placed in a short distance after the water aquarium (see Figure 1). In general, the distance of the cold spot is larger for markers that induce smaller scattering angles, and the magnitude is then smaller. Therefore, the maximum cold spots for the  $\text{ZrO}_2$  marker appear after the water aquarium (compare Table 4 and Figure 1). The WEPL of the sensors and the air gaps in-between were estimated to be  $< 1$  mm in total, which has little influence on the results. If the air gap before the sensor would be replaced by water, the magnitude of the cold spot would be slightly but not significantly suppressed and the distance from the marker would also decrease a little. For the Gold Anchor and the Viscoil markers, the positions of the cold spots were found to be inside the water aquarium, which means that they would not be different if the water aquarium would be larger.

The cold spots evaluated with radiochromic films in previous studies (Cheung et al. 2010, Huang et al. 2011) for protons were bigger than the ones found in this work. This was expected since the multiple Coulomb scattering is stronger for protons than  $^{12}\text{C}$  ions. In addition, the small gold markers investigated by Cheung et al. (2010) had a diameter of 0.8 mm that is bigger compared to the ones studied in this work with a maximum diameter of 0.5 mm.

For the film measurements, the beam intensities are generally in the order of  $10^7$ – $10^8$  particles/s which means that after some seconds, the measurement is done. For the case of the MIMOSA28 sensors, the beam intensity needs to be decreased to  $10^3$ – $10^4$  particles/s to avoid pile-up in the detectors which leads to longer measurement times. Each measurement was about 1 hour and the low particle rates can lead in some cases to a lack of statistics. For instance, precisely quantifying the cold spot of the Gold Anchor #2 which has a complex geometry and a smaller integrated area was difficult within the measurement time. However, as shown in Figure 8, the structure of this fiducial marker creates several cold spots.

As investigated in this work, the perturbation is more important for lower energy beams since the scattering is stronger. The absorbed dose is proportional to the fluence and the Linear Energy Transfer (LET). The latter varies along the particle path and is higher for

low energies. This implies that the dose perturbation is stronger if the created cold spot appears to be in the Bragg peak region. For heavy ions (e.g. carbon ions), fragments of lower  $Z$  than the primary beam are produced forming then the fragmentation tail of the Bragg curve. These fragments are scattered as well by the markers and contribute to the dose perturbation. However, they do not have a major impact compared to the primary ions.

The perturbations in this work were measured with markers positioned in a perpendicular orientation with respect to the beam axis and show cold spot results from less than 3% up to 9%. As studied from Newhauser et al. (2007), the orientation of the marker has an impact on the dose perturbation. The magnitude of the perturbation is stronger for a parallel orientation of the marker with respect to the beam axis resulting from a larger thickness of the scattering material. On the other hand, the volume of the perturbation becomes smaller. Within the available beam time of our measurements we focused on the more likely case where the markers are not parallel to the beam. In a future work, the effect of different marker orientations could also be examined with the presented setup. From a clinical point of view, the perturbations should be considered if the markers used for image guidance have a high atomic number and a diameter  $> 0.5$  mm. However, to give a clear statement about the clinical impact, it is necessary to include all parameters contributing to the dose perturbations. The latter depend on the type of markers used and their position inside the tumor, the type of particle and its energy and the irradiation fields used for the patient treatment. In addition, it is very difficult to assess the clinical impact of the dose perturbations that also depends on complicated tissue effects. However, there is a potential risk from the cold spots for a locale recurrence of the tumor. Therefore, it is one goal of this work to quantify and compare the effect on the dose for different markers in a sense that there is less or more risk.

It is also important to note that the perturbations measured in this work are due to an edge-scattering effect from the markers and not due to a range shift. The created cold spots were quantified in this work. The hot spots were not investigated in this study but could be measured as well as their position in order to verify that they are not produced inside unwanted tissues such as an OAR. In a future work, the setup could be improved where the sensors would be placed inside the water aquarium and using a scanned beam to have a homogeneous field instead of a Gaussian beam spot.

## 5. Conclusion

In this work, fluence perturbations due to edge-scattering effects could be evaluated for several small fiducial markers used during ion-beam therapy for patient positioning verification. The studied markers were composed of different materials and had different geometries. In this study, a new concept was proposed and validated to study the fluence perturbations creating cold and hot spots after fiducial markers. A tracker system composed of six MIMOSA28 pixel sensors was used to measure the trajectory of each

single particle and reconstruct a 3D fluence distribution with high spatial resolution from all tracks. The maximum cold spots created after the fiducial markers could be quantified as well as their longitudinal position after computing the 2D fluence map. This measurement method was validated against the standard measurement method using radiochromic films. The measurements showed that the fluence perturbations due to edge-scattering effects can be significantly reduced when low density and low atomic number materials are used such as the carbon-coated  $\text{ZrO}_2$  marker instead of the gold ones. Therefore, such markers should be preferred for carbon ion treatments if the imaging method used for positioning can display them. With the use of a tracker system, the maximum cold spots from fiducial markers could be determined without knowing in advance their position along the beam axis which makes this measurement concept superior compared to radiochromic films. The measurement of the fluence perturbation with this new method should also be done for other therapy beams, especially light ions such as protons or helium ions since they scatter differently compared to carbon beams. The experimental data from this study can be useful for the benchmarking of MC codes.

### Acknowledgements

The experiments conducted at the Marburg Ion Therapy Center for this work were funded by *Hessisches Ministerium für Wissenschaft und Kunst* within the *Förderprogramm MIT-Forschung*. We thank Yannick Senger, Matthias Witt and the accelerator staff for the help and organization during the beam time campaign. We would like to thank the mechanical workshop at GSI for their help for building an improved mechanical setup.

## REFERENCES

20

## References

- Agostinelli, S., Allison, J., Amako, K. a., Apostolakis, J., Araujo, H., Arce, P., Asai, M., Axen, D., Banerjee, S., Barrand, G. . et al. (2003), 'GEANT4: A Simulation toolkit', *Nucl. Instrum. Meth.* **A506**, 250–303.
- Balter, J. M., Sandler, H. M., Lam, K., Bree, R. L., Lichter, A. S. & Ten Haken, R. K. (1995), 'Measurement of prostate movement over the course of routine radiotherapy using implanted markers', *International Journal of Radiation Oncology\* Biology\* Physics* **31**(1), 113–118.
- Borca, V. C., Pasquino, M., Russo, G., Grosso, P., Cante, D., Sciacero, P., Girelli, G., Porta, M. R. L. & Tofani, S. (2013), 'Dosimetric characterization and use of GAFCHROMIC EBT3 film for IMRT dose verification', *Journal of applied clinical medical physics* **14**, 158–171.
- Brun, R. & Rademakers, F. (1996), ROOT - An Object Oriented Data Analysis Framework, in 'AIHENP'96 Workshop, Lausanne', Vol. 389, pp. 81–86.
- Cheung, J., Kudchadker, R. J., Zhu, X. R., Lee, A. K. & Newhauser, W. D. (2010), 'Dose perturbations and image artifacts caused by carbon-coated ceramic and stainless steel fiducials used in proton therapy for prostate cancer', *Physics in Medicine & Biology* **55**(23), 7135.
- Crook, J., Raymond, Y., Salhani, D., Yang, H. & Esche, B. (1995), 'Prostate motion during standard radiotherapy as assessed by fiducial markers', *Radiotherapy and oncology* **37**(1), 35–42.
- Finck, C., Karakaya, Y., Reithinger, V., Rescigno, R., Baudot, J., Constanzo, J., Juliani, D., Krimmer, J., Rinaldi, I., Rousseau, M. et al. (2017), 'Study for online range monitoring with the interaction vertex imaging method', *Physics in Medicine & Biology* **62**(24), 9220.
- Giebeler, A., Fontenot, J., Balter, P., Ciangaru, G., Zhu, R. & Newhauser, W. (2009), 'Dose perturbations from implanted helical gold markers in proton therapy of prostate cancer', *Journal of applied clinical medical physics* **10**(1), 63–70.
- Habermehl, D., Henkner, K., Ecker, S., Jäkel, O., Debus, J. & Combs, S. E. (2013), 'Evaluation of different fiducial markers for image-guided radiotherapy and particle therapy', *Journal of radiation research* **54**(suppl.1), i61–i68.
- Herrmann, R., Carl, J., Jäkel, O., Bassler, N. & Petersen, J. B. (2010), 'Investigation of the dosimetric impact of a ni-ti fiducial marker in carbon ion and proton beams', *Acta Oncologica* **49**(7), 1160–1164.
- Highland, V. L. (1975), 'Some practical remarks on multiple scattering', *Nuclear Instruments and Methods* **129**(2), 497 – 499.
- Highland, V. L. (1979), 'Erratum', *Nuclear Instruments and Methods* **161**(1), 171.
- Huang, J. Y., Newhauser, W. D., Zhu, X. R., Lee, A. K. & Kudchadker, R. J. (2011), 'Investigation of dose perturbations and the radiographic visibility of potential

## REFERENCES

21

- fiducials for proton radiation therapy of the prostate', *Physics in Medicine & Biology* **56**(16), 5287.
- Kupelian, P. A., Willoughby, T. R., Meeks, S. L., Forbes, A., Wagner, T., Maach, M. & Langen, K. M. (2005), 'Intraprostatic fiducials for localization of the prostate gland: monitoring intermarker distances during radiation therapy to test for marker stability', *International Journal of Radiation Oncology\* Biology\* Physics* **62**(5), 1291–1296.
- León-Marroquín, E. Y., Lárraga-Gutiérrez, J. M., Herrera-González, J. A., Camacho-López, M. A., Villarreal Barajas, J. E. & García-Garduño, O. A. (2018), 'Investigation of EBT3 radiochromic film's response to humidity', *Journal of applied clinical medical physics* **19**, 283–290.
- Matsuura, T., Maeda, K., Sutherland, K., Takayanagi, T., Shimizu, S., Takao, S., Miyamoto, N., Nihongi, H., Toramatsu, C., Nagamine, Y. et al. (2012), 'Biological effect of dose distortion by fiducial markers in spot-scanning proton therapy with a limited number of fields: A simulation study', *Medical physics* **39**(9), 5584–5591.
- Newhauser, W., Fontenot, J., Koch, N., Dong, L., Lee, A., Zheng, Y., Waters, L. & Mohan, R. (2007), 'Monte carlo simulations of the dosimetric impact of radiopaque fiducial markers for proton radiotherapy of the prostate', *Physics in Medicine & Biology* **52**(11), 2937–2952.
- Reidel, C.-A., Finck, C., Schuy, C., Rovituso, M. & Weber, U. (2019), 'Alignment procedure of silicon pixel detectors for ion-beam therapy applications', *Nucl. Inst. & Meth. in Phys. Res. A* **931**.
- Rescigno, R., Finck, C., Juliani, D., Spiriti, E., Baudot, J., Abou-Haidar, Z., Agodi, C., Álvarez, M. A. G., Aumann, T., Battistoni, G. et al. (2014), 'Performance of the reconstruction algorithms of the FIRST experiment pixel sensors vertex detector', *Nucl. Instrum. Meth.* **A767**, 34 – 40.
- Schardt, D., Elsässer, T. & Schulz-Ertner, D. (2010), 'Heavy-ion tumor therapy: Physical and radiobiological benefits', *Reviews of modern physics* **82**(1), 383.
- Schneider, C. A., Rasband, W. S. & Eliceiri, K. W. (2012), 'Nih image to imagej: 25 years of image analysis', *Nature methods* **9**(7), 671.
- Schoenfeld, A. A., Wieker, S., Harder, D. & Poppe, B. (2016), 'The origin of the flatbed scanner artifacts in radiochromic film dosimetry—key experiments and theoretical descriptions', *Physics in Medicine and Biology* **61**, 7704–7724.
- Spiriti, E., Finck, C., Baudot, J., Divay, C., Juliani, D., Labalme, M., Rousseau, M., Salvador, S., Vanstalle, M., Agodi, C. et al. (2017), 'CMOS active pixel sensors response to low energy light ions', *Nucl. Instrum. Meth.* **A875**, 35–40.
- Tarasov, O. & Bazin, D. (2008), 'Lise++: Radioactive beam production with in-flight separators', *Nuclear Instruments and Methods in Physics Research Section B: Beam Interactions with Materials and Atoms* **266**(19-20), 4657–4664.

## REFERENCES

22

- 1  
2  
3  
4  
5 Ten Haken, R., Forman, J., Heimburger, D., Gerhardsson, A., McShan, D., Perez-  
6 Tamayo, C., Schoepfel, S. & Lichter, A. (1991), 'Treatment planning issues related  
7 to prostate movement in response to differential filling of the rectum and bladder',  
8 *International Journal of Radiation Oncology\* Biology\* Physics* **20**(6), 1317–1324.  
9  
10 Valin, I., Hu-Guo, C., Baudot, J., Bertolone, G., Besson, A., Colledani, C., Claus, G.,  
11 Dorokhov, A., Dozière, G., Dulinski, W. et al. (2012), 'A reticle size CMOS pixel  
12 sensor dedicated to the STAR HFT', *Journal of Instrumentation* **7**(01), C01102.  
13  
14  
15  
16  
17  
18  
19  
20  
21  
22  
23  
24  
25  
26  
27  
28  
29  
30  
31  
32  
33  
34  
35  
36  
37  
38  
39  
40  
41  
42  
43  
44  
45  
46  
47  
48  
49  
50  
51  
52  
53  
54  
55  
56  
57  
58  
59  
60